Chapter 3

CONSERVATION LAWS WITH SPATIALLY VARYING FLUX FUNCTIONS

In the previous chapter we introduced a class of wave propagation algorithms for conservation laws with autonomous flux functions of the form $\boldsymbol{f}(\boldsymbol{q})$. In Chapter 1, however, we mentioned that conservation laws written in a general basis (i.e. a basis that covers a manifold $\mathscr{M}$) have flux functions that depend explicitly on the spatial coordinates x^k. The general form of such a conservation law is shown in equation (1.4), and a derivation of the functional form of the flux for this equation follows in Chapter 5.

Spatially-varying flux functions are not unique to conservation laws on manifolds, but arise in many different applications. An application to a problem in numerical relativity is discussed by Bardeen and Buchman [7]. Spatially-varying flux functions also arise in the modeling of traffic flow on roads with varying conditions, nonlinear elasticity in heterogeneous materials, or flow through a heterogeneous porous media.

In this chapter we present a general approach to solving conservation laws with spatially-varying flux functions. The method is based on solving modified Riemann problems that give rise to a new set of waves that are called f-waves. In Chapter 6 we will use this approach to handle the spatial variation that appears on manifolds. This chapter is based on a paper by Bale, LeVeque, Mitran, and Rossmanith [4].

3.1 The f-wave decomposition

In one space dimension the equation for a conservation law with a spatially-varying flux function has the form

$$\boldsymbol{q}_{,t} + \boldsymbol{f}(\boldsymbol{q}, x)_{,x} = 0, \tag{3.1}$$

where $\boldsymbol{q}$ is again a vector of state variables and $\boldsymbol{f}(\boldsymbol{q}, x) : \mathbb{R}^{n_{\text{eq}}} \times \mathbb{R} \to \mathbb{R}^{n_{\text{eq}}}$ is the flux. Recall that in equation (2.1) the grid function $\boldsymbol{Q}_i$ represents the finite volume approximation of $\boldsymbol{q}$ in each cell. Similarly, for a flux function that depends on a spatial variable we assume a cell-centered piecewise constant discretization such that $\boldsymbol{f}_i(\boldsymbol{q})$ is the value of the flux throughout the i^{th} grid cell. Any discretization consistent with a finite volume representation will work, for example $\boldsymbol{f}_i(\boldsymbol{q}) = \boldsymbol{f}(\boldsymbol{q}, x_i)$. Using this cell-centered approximation to the flux, the generalized Riemann problem at the cell interface $x = x_{i-1/2}$ consists of the equation

$$\boldsymbol{q}_{,t} + \mathcal{F}_{i-1/2}(\boldsymbol{q}, x)_{,x} = 0, \tag{3.2}$$

where

$$\mathcal{F}_{i-1/2}(\boldsymbol{q}, x) = \begin{cases} \boldsymbol{f}_{i-1}(\boldsymbol{q}) & \text{if } x < x_{i-1/2} \\ \boldsymbol{f}_i(\boldsymbol{q}) & \text{if } x > x_{i-1/2}, \end{cases} \tag{3.3}$$

together with initial data (2.9) with $\boldsymbol{q}_l = \boldsymbol{Q}_{i-1}$ and $\boldsymbol{q}_r = \boldsymbol{Q}_i$.

At each cell interface, the generalized Riemann problem (3.2) is solved using the eigenvectors of a matrix $A_{i-1/2}$ that approximates the Jacobian $\partial \boldsymbol{f}/\partial \boldsymbol{q}(\boldsymbol{q}, x)$. Typically, for the standard wave propagation algorithm based on splitting jumps in $\boldsymbol{Q}$, $A_{i-1/2}$ uses Roe averages (i.e. see [69]) to ensure that equation (2.35) is satisfied and the method remains conservative. One of the features of the approach presented here is that the update will remain conservative for any reasonable choice of $A_{i-1/2}$, making it no longer necessary to compute Roe averages. For simple systems this is not very beneficial, but for complicated systems like that of magneto-hydrodynamics, the Roe average is difficult to find and expensive to compute.

The approximate Jacobian can be left quite general so that

$$A_{i-1/2} = A(\boldsymbol{Q}_{i-1}, x_{i-1}, \boldsymbol{Q}_i, x_i), \tag{3.4}$$

where A is some matrix-valued function that approximates the Jacobian. It will be shown in Section 3.3 that, provided $\boldsymbol{q}(t, x)$ and $\boldsymbol{f}(\boldsymbol{q}, x)$ remain smooth, the wave propagation algorithm presented here is second order if A approximates the Jacobian so that

$$A\left(\boldsymbol{q}(t, x-\Delta x), x-\Delta x, \boldsymbol{q}(t, x), x\right) = \frac{\partial \boldsymbol{f}}{\partial \boldsymbol{q}}\left(\boldsymbol{q}\left(t, x-\frac{\Delta x}{2}\right), x-\frac{\Delta x}{2}\right) + E(x, \Delta x), \tag{3.5}$$

where the error $E(x, \Delta x)$ satisfies

$$E(x, \Delta x) = \mathcal{O}(\Delta x) \quad \text{as } \Delta x \to 0 \tag{3.6}$$

and

$$\frac{E(x, \Delta x) - E(x-\Delta x, \Delta x)}{\Delta x} = \mathcal{O}(\Delta x) \quad \text{as } \Delta x \to 0. \tag{3.7}$$

Another discussion of the accuracy of this approach applied to gravitational plane waves in general relativity can be found in [7]. For a particular choice of $A_{i-1/2}$, the nonlinear problem (3.2) is replaced by a linear one with

$$\boldsymbol{q}_{,t} + A_{i-1/2}\, \boldsymbol{q}_{,x} = 0. \tag{3.8}$$

We have seen how to solve the linear problem in Section 2.2.1.

The matrix $A_{i-1/2}$ is never constructed explicitly since only its set of eigenvalues $\{\lambda^p\}$ and eigenvectors $\{\boldsymbol{r}^p\}$ are needed in the solution of the Riemann problem. In practice there are various approaches to choose the eigenvectors. For example, one way is to choose the eigenvectors of $\partial \boldsymbol{f}_{i-1}(\boldsymbol{Q}_{i-1}, x_{i-1})/\partial \boldsymbol{q}$ that correspond to the negative eigenvalues and therefore left-propagating waves, and combine these with eigenvectors of $\partial \boldsymbol{f}_i(\boldsymbol{Q}_i, x_i)/\partial \boldsymbol{q}$ that correspond to positive eigenvalues. Another way is to choose the eigenvectors of the Jacobian $\partial \boldsymbol{f}/\partial \boldsymbol{q}(\overline{\boldsymbol{Q}}_{i-1/2}, x_{i-1/2})$ evaluated at some average $\overline{\boldsymbol{Q}}_{i-1/2}$ of the states to the left and right of the interface. This average may be a simple arithmetic average, or a more complicated average like a Roe average.

It was shown in Section 2.2.1 that the Riemann solution for the constant coefficient linear system (3.8) can be written as a superposition of waves $\boldsymbol{\mathcal{W}}_{i-1/2}$. The standard wave propagation algorithm defines waves by decomposing the jump in $\boldsymbol{Q}$ across the interface

$$\boldsymbol{Q}_i - \boldsymbol{Q}_{i-1} = \sum_{p=1}^{n_{eq}} \alpha^p_{i-1/2}\, \boldsymbol{r}^p_{i-1/2} = \sum_{p=1}^{n_{eq}} \boldsymbol{\mathcal{W}}^p_{i-1/2}, \tag{3.9}$$

where

$$\alpha^p = \boldsymbol{l}^p \cdot \left(\boldsymbol{Q}_i - \boldsymbol{Q}_{i-1}\right). \tag{3.10}$$

These waves are then used to construct the fluctuations (2.26) that are used in the one-dimensional update (2.31) or the multidimensional update (2.52). Recall, however, that the updates (2.31) and (2.52) for the linear system (3.8) are only conservative if the condition (2.35) is satisfied implying that

$$\boldsymbol{f}(\boldsymbol{Q}_i) - \boldsymbol{f}(\boldsymbol{Q}_{i-1}) = \sum_{p=1}^{n_{eq}} \alpha^p_{i-1/2}\, s^p_{i-1/2}\, \boldsymbol{r}^p_{i-1/2} \tag{3.11}$$

is true across each interface $x = x_{i-1/2}$.

As was previously stated, a novel feature of the algorithm presented in this chapter is that any attempts to define a Jacobian matrix $A_{i-1/2}$ such that the condition (**??**), and equivalently equation (2.35), is satisfied are abandoned. A classical decomposition of the jump in $\boldsymbol{Q}$ across the interface at $x = x_{i-1/2}$ is not used to solve the Riemann problem. Instead, the flux-based decomposition

$$\boldsymbol{f}_i(\boldsymbol{Q}_i) - \boldsymbol{f}_{i-1}(\boldsymbol{Q}_{i-1}) = \sum_{p=1}^{n_{eq}} \beta^p_{i-1/2}\, \boldsymbol{r}^p_{i-1/2} \equiv \sum_{p=1}^{n_{eq}} \boldsymbol{\mathcal{Z}}^p_{i-1/2}, \tag{3.12}$$

where

$$\beta^p_{i-1/2} = \boldsymbol{l}^p_{i-1/2} \cdot \left(\boldsymbol{f}_i(\boldsymbol{Q}_i) - \boldsymbol{f}_{i-1}(\boldsymbol{Q}_{i-1})\right) \tag{3.13}$$

is used to construct the solution. This decomposition defines a set of f-waves $\{\boldsymbol{\mathcal{Z}}_{i-1/2}\}$ at the interface. In the following section we demonstrate that the set of f-waves are in fact the natural set of waves to use for spatially-varying flux functions. In Section 3.3 we present a modified wave propagation algorithm that makes use of these f-waves.

3.2 The generalized Riemann problem

It will be shown in this section that it is the f-waves that yield the correct solution to the generalized Riemann problem (3.2) associated with a spatially-varying flux function. As in Section 2.3.1 the advection equation is considered, but the velocity will now depend on x so that the equation has the form

$$q_{,t} + \left(u(x)\, q(t,x)\right)_{,x} = 0. \tag{3.14}$$

The discretization for the flux is naturally taken to be $f_i(q) = u(x_i)\, q \equiv u_i\, q$, where u_i is the advection velocity in the i^{th} cell. Assuming that u_i does not change sign across the interface, the structure of the Riemann solution (for $u_i > 0$) is shown in Figure 3.1(a) and is comprised of a single propagating wave $\boldsymbol{\mathcal{W}}^1_{i-1/2}$ with speed u_i and strength $Q_i - Q^r_{i-1/2}$, together with a stationary discontinuity at $x = x_{i-1/2}$ with amplitude $Q^r_{i-1/2} - Q_{i-1}$. The stationary discontinuity exists due to the fact that for bounded solutions of equation (3.1), it is expected that the flux will be continuous across the interface so that

$$u_{i-1}\, Q_{i-1} = u_i\, Q^r_{i-1/2}, \tag{3.15}$$

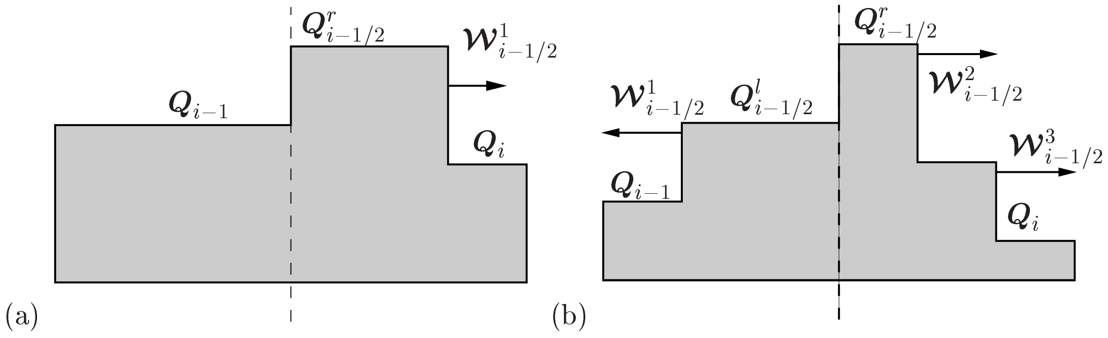

Figure 3.1: (a) The solution to the generalized Riemann problem for the advection equation consists of a traveling wave $\boldsymbol{\mathcal{W}}^1_{i-1/2}$ and a stationary jump in $\boldsymbol{Q}$ across the interface $x = x_{i-1/2}$. (b) The solution for a system of equations also contains a stationary jump.

which sets the necessary amplitude for the value of $Q^r_{i-1/2}$ just to the right of the interface. The solution to the generalized Riemann problem can then be written as

$$q(t,x) = \begin{cases} Q_{i-1} & \text{for } x < x_{i-1/2} \\ Q^r_{i-1/2} & \text{for } x_{i-1/2} < x < x_{i-1/2} + u_i\,(t - t_n) \\ Q_i & \text{for } x > x_{i-1/2} + u_i\,(t-t_n), \end{cases} \tag{3.16}$$

where

$$Q^r_{i-1/2} = \frac{u_{i-1}}{u_i}\, Q_{i-1} \tag{3.17}$$

is the value of q in the spacetime wedge between the lines $x = x_{i-1/2}$ and $x = x_{i-1/2} + u_i\,(t - t_n)$.

Suppose that the classical decomposition (3.9) was used to to generate the waves used to solve the Riemann problem just discussed. Define the Jacobian $A_{i-1/2} = u_i$ (once again for $u_i > 0$) with $\boldsymbol{r}^1_{i-1/2} = 1$ and $s^1_{i-1/2} = u_i$. The wave is then defined by

$$\boldsymbol{\mathcal{W}}^1_{i-1/2} = \alpha^1_{i-1/2} = Q_i - Q_{i-1}, \tag{3.18}$$

and will propagate at a speed $s^1_{i-1/2} = u_i$. In this case, the wave strength is the entire jump $Q_i - Q_{i-1}$ leaving no stationary discontinuity at $x = x_{i-1/2}$. This is not the correct Riemann solution since there is jump $Q_{i-1}(f_i(Q_i) - f_{i-1}(Q_{i-1})$ in the flux that remains at the interface.

If instead, the flux-based decomposition (3.12) is used with the same definition of the Jacobian, then

$$\mathcal{Z}^1_{i-1/2} = \beta^1_{i-1/2} = u_i\, Q_i - u_{i-1}\, Q_{i-1}. \tag{3.19}$$

The strength of the traveling wave from Figure 3.1(a) can be recovered by dividing the

f-wave by $s^1_{i-1/2}$

$$\begin{aligned}\mathcal{W}^1_{i-1/2} &= \mathcal{Z}^1_{i-1/2}/s^1_{i-1/2}\\ &= \left(u_i\, Q_i - u_{i-1}\, Q_{i-1}\right)/u_i \\ &= Q_i - Q^r_{i-1/2},\end{aligned} \tag{3.20}$$

just as should be expected. It is also true that the f-wave carries the entire jump in the flux so that no discontinuity in the flux remains at the interface.

For systems of equations the solution of the generalized Riemann problem has a structure depicted in Figure 3.1(b). There will be n_{eq} waves $\boldsymbol{\mathcal{W}}^p_{i-1/2}$ traveling at speeds $\boldsymbol{s}^p_{i-1/2}$, and a stationary jump in $\boldsymbol{q}$ at $x = x_{i-1/2}$ with strength $\boldsymbol{Q}^r_{i-1/2} - \boldsymbol{Q}^l_{i-1/2}$. Once again, if equation (3.1) is expected to have a bounded solution then the flux will be continuous across the interface $x = x_{i-1/2}$ so that

$$\boldsymbol{f}_{i-1}(\boldsymbol{Q}^l_{i-1/2}) = \boldsymbol{f}_i(\boldsymbol{Q}^r_{i-1/2}). \tag{3.21}$$

This condition can be used to calculate the jump across the stationary discontinuity at $x = x_{i-1/2}$.

3.3 Wave propagation algorithms using the f-waves

The formulas presented in Section 2.3 are easily modified to make use of the set of f-waves, $\{\boldsymbol{\mathcal{Z}}^p_{i-1/2}\}$, instead of the standard set of waves, $\{\boldsymbol{\mathcal{W}}^p_{i-1/2}\}$. Since $\boldsymbol{\mathcal{Z}}^p_{i-1/2} = s^p_{i-1/2}\,\boldsymbol{\mathcal{W}}^p_{i-1/2}$, the fluctuations (2.26) are replaced with

$$\boldsymbol{\mathcal{A}}^{\pm}\boldsymbol{\Delta Q}_{i-1/2} = \sum_{p\in\mathscr{P}^{\pm}} \boldsymbol{\mathcal{Z}}^p_{i-1/2}, \tag{3.22}$$

where as before, $\mathscr{P}^-$ is the set of p for which $s^p_{i-1/2} < 0$ and similarly, $\mathscr{P}^+$ is the set for which $s^p_{i-1/2} > 0$.

The correction flux (2.41) can be replaced with

$$\tilde{\boldsymbol{F}}_{i-1/2} = \frac{1}{2}\sum_{p=1}^{n_{eq}} \operatorname{sgn}(s^p_{i-1/2})\left(1 - \frac{\Delta t}{\Delta x}|s^p_{i-1/2}|\right)\tilde{\boldsymbol{\mathcal{Z}}}^p_{i-1/2}, \tag{3.23}$$

where the tilde implies that a limiter is used. The limiters are applied directly to the f-waves so that

$$\tilde{\boldsymbol{\mathcal{Z}}}^p_{i-1/2} = \text{Limiter}(\boldsymbol{\mathcal{Z}}^p_{i-1/2}, \boldsymbol{\mathcal{Z}}^p_{I-1/2}), \tag{3.24}$$

with

$$I = \begin{cases} i-1 & \text{if } s^p_{i-1/2} > 0 \\ i+1 & \text{if } s^p_{i+1/2} > 0, \end{cases} \tag{3.25}$$

just as for the standard waves. For linear problems it can be shown that the first order algorithm based on f-waves reduces to the standard algorithm. The high-resolution corrections, however, are different due to the fact that the limiters are applied directly to the f-waves.

Since standard waves must be defined in terms of f-waves as $\boldsymbol{\mathcal{W}}^p_{i-1/2} = \boldsymbol{\mathcal{Z}}^p_{i-1/2}/s^p_{i-1/2}$, the fact that the high-resolution correction can be implemented in terms of the f-waves directly avoids problems when $s^p_{i-1/2} = 0$. Using the fluctuations (3.22), and the correction fluxes (3.23), the high-resolution wave propagation update becomes

$$\begin{aligned} \boldsymbol{Q}_i^{n+1} = \boldsymbol{Q}_i^n &- \frac{\Delta t}{\Delta x}\left(\boldsymbol{\mathcal{A}}^+\boldsymbol{\Delta Q}_{i-1/2} + \boldsymbol{\mathcal{A}}^-\boldsymbol{\Delta Q}_{i+1/2}\right) \\ &- \frac{\Delta t}{\Delta x}\left(\tilde{\boldsymbol{F}}_{i+1/2} - \tilde{\boldsymbol{F}}_{i-1/2}\right). \end{aligned} \tag{3.26}$$

This update looks identical to the standard update, but fluctuations and correction fluxes are computed using f-waves.

It was previously stated that the algorithm presented here would be second order provided that the solution, $\boldsymbol{q}(t,x)$, and flux function, $f(\boldsymbol{q},x)$, remain smooth and the conditions (3.6) and (3.7) on the approximate Jacobian are satisfied. To show this, consider the update (3.26) without limiters so that

$$\begin{aligned} \boldsymbol{Q}_i^{n+1} = \boldsymbol{Q}_i^n \quad &- \tfrac{\Delta t}{\Delta x} \left[\sum_{p\in\mathscr{P}^+} \boldsymbol{\mathcal{Z}}^p_{i-1/2} + \sum_{p\in\mathscr{P}^-} \boldsymbol{\mathcal{Z}}^p_{i+1/2}\right] \\ &- \tfrac{\Delta t}{2\Delta x} \left[\sum_{p=1}^{n_{eq}} \operatorname{sign}(s^p_{i+1/2})\left(1 - \frac{\Delta t}{\Delta x}\left|s^p_{i+1/2}\right|\right)\boldsymbol{\mathcal{Z}}^p_{i+1/2}\right. \\ &\qquad \left. - \sum_{p=1}^{n_{eq}} \operatorname{sign}(s^p_{i-1/2})\left(1 - \frac{\Delta t}{\Delta x}\left|s^p_{i-1/2}\right|\right)\boldsymbol{\mathcal{Z}}^p_{i-1/2}\right] \end{aligned} \tag{3.27}$$

$$\begin{aligned} = \boldsymbol{Q}_i^n \quad &- \tfrac{\Delta t}{\Delta x} \left[\sum_{p\in\mathscr{P}^+} \boldsymbol{\mathcal{Z}}^p_{i-1/2} - \frac{1}{2}\sum_{p=1}^{n_{eq}} \operatorname{sign}(s^p_{i-1/2})\boldsymbol{\mathcal{Z}}^p_{i-1/2}\right. \\ &\qquad \left. + \sum_{p\in\mathscr{P}^-} \boldsymbol{\mathcal{Z}}^p_{i+1/2} + \frac{1}{2}\sum_{p=1}^{n_{eq}} \operatorname{sign}(s^p_{i+1/2})\boldsymbol{\mathcal{Z}}^p_{i+1/2}\right] \\ &+ \tfrac{\Delta t^2}{2\Delta x^2} \left[\sum_{p=1}^{n_{eq}} \operatorname{sign}(s^p_{i+1/2})\left|s^p_{i+1/2}\right|\boldsymbol{\mathcal{Z}}^p_{i+1/2}\right. \\ &\qquad \left. - \sum_{p=1}^{n_{eq}} \operatorname{sign}(s^p_{i-1/2})\left|s^p_{i-1/2}\right|\boldsymbol{\mathcal{Z}}^p_{i-1/2}\right], \end{aligned} \tag{3.28}$$

where all that has been done is a gathering of the powers in $\Delta t/\Delta x$. In this reordering, the first order fluctuations have gained terms that will convert upwind differences to central differences. The previous expression can be simplified by eliminating the sign$(\cdot)$ functions. The following relationships:

$$\begin{aligned} \sum_{p=1}^{n_{eq}} \operatorname{sign}(s^p_I)\boldsymbol{\mathcal{Z}}^p_I &= \sum_{p\in\mathscr{P}^+} \boldsymbol{\mathcal{Z}}^p_I - \sum_{p\in\mathscr{P}^-} \boldsymbol{\mathcal{Z}}^p_I, \\ \operatorname{sign}(s^p_I)\left|s^p_I\right| &= s^p_I, \end{aligned} \tag{3.29}$$

for $I = i \pm 1/2$ can be used in equation (3.28) to get

$$\begin{aligned} \boldsymbol{Q}_i^{n+1} = \boldsymbol{Q}_i^n \quad & -\tfrac{\Delta t}{\Delta x} \quad \left[\sum_{p=1}^{n_{eq}} \boldsymbol{\mathcal{Z}}_{i-1/2}^p + \sum_{p=1}^{n_{eq}} \boldsymbol{\mathcal{Z}}_{i+1/2}^p \right] \\ & -\tfrac{\Delta t}{2\Delta x} \quad \left[\sum_{p=1}^{n_{eq}} s_{i+1/2}^p \boldsymbol{\mathcal{Z}}_{i+1/2}^p - \sum_{p=1}^{n_{eq}} s_{i+1/2}^p \boldsymbol{\mathcal{Z}}_{i+1/2}^p \right]. \end{aligned} \tag{3.30}$$

The last line in the previous update can be related to the approximate Jacobian using

$$\sum_{p=1}^{n_{eq}} s_I^p \boldsymbol{\mathcal{Z}}_I^p = A_I \sum_{p=1}^{n_{eq}} \boldsymbol{\mathcal{Z}}_I^p, \tag{3.31}$$

since s_I^p is an eigen value of the matrix A_I with the corresponding eigenvector $\boldsymbol{\mathcal{Z}}_I^p$. The resulting update has the form

$$\begin{aligned} \boldsymbol{Q}_i^{n+1} = \boldsymbol{Q}_i^n \quad & -\tfrac{\Delta t}{\Delta x} \quad \left[\sum_{p=1}^{n_{eq}} \boldsymbol{\mathcal{Z}}_{i-1/2}^p + \sum_{p=1}^{n_{eq}} \boldsymbol{\mathcal{Z}}_{i+1/2}^p \right] \qquad (3.32) \\ & -\tfrac{\Delta t}{2\Delta x} \quad \left[A_{i+1/2} \sum_{p=1}^{n_{eq}} \boldsymbol{\mathcal{Z}}_{i+1/2}^p - A_{i-1/2} \sum_{p=1}^{n_{eq}} \boldsymbol{\mathcal{Z}}_{i+1/2}^p \right]. \\ = \boldsymbol{Q}_i^n \quad & -\tfrac{\Delta t}{2\Delta x} \quad \big(\boldsymbol{f}(\boldsymbol{Q}_{i+1}^n, x_{i+1}) - \boldsymbol{f}(\boldsymbol{Q}_{i-1}^n, x_{i-1}) \big) \qquad (3.33) \\ & -\tfrac{\Delta t^2}{2\Delta x^2} \quad \Big[A_{i+1/2} \big(\boldsymbol{f}(\boldsymbol{Q}_{i+1}^n, x_{i+1}) - \boldsymbol{f}(\boldsymbol{Q}_i^n, x_i) \big) \\ & \qquad - A_{i-1/2} \big(\boldsymbol{f}(\boldsymbol{Q}_i^n, x_i) - \boldsymbol{f}(\boldsymbol{Q}_{i-1}^n, x_{i-1}) \big) \Big], \end{aligned}$$

where in the last equality we have used equation (3.12) that states the entire flux difference is carried by the f-waves at each cell interface.

The Taylor series expansion for the true solution has the form

$$\begin{aligned} \boldsymbol{q}(t_{n+1}, x_i) = \boldsymbol{q}(t,x)|_{t_n,x_i} & - \Delta t \, \boldsymbol{f}(\boldsymbol{q},x)_{,x}|_{t_n,x_i} \\ & + \frac{1}{2} \Delta t^2 \left[\partial \boldsymbol{f} / \partial \boldsymbol{q} \, (q,x) \, \boldsymbol{f}(\boldsymbol{q},x)_{,x} \right]_{,x} |_{t_n,x_i} + \mathcal{O}(\Delta t^3). \end{aligned} \tag{3.34}$$

The $\mathcal{O}(\Delta t)$ terms of the update (3.33) and the Taylor expansion agree to $\mathcal{O}(\Delta t \, \Delta x^2)$. The conditions that the approximate Jacobian satisfy, namely (3.6) and (3.7), allow us to write

$$\begin{aligned} A(\boldsymbol{q}(t,x-\Delta x), \boldsymbol{q}(t,x)) \left(\frac{\boldsymbol{f}(\boldsymbol{q}(t,x),x) - \boldsymbol{f}(\boldsymbol{q}(t,x-\Delta x), x-\Delta x)}{\Delta x} \right) = \\ \partial \boldsymbol{f} / \partial \boldsymbol{q} \, (\boldsymbol{q}(t, x-\Delta x/2), x-\Delta x)[\\ \boldsymbol{f}(\boldsymbol{q}(t,x-\Delta x/2), x-\Delta x/2)]_{,x} + E_2(x,\Delta x), \end{aligned} \tag{3.35}$$

and guarantee that $E_2(x, \Delta x)$ is at least $\mathcal{O}(\Delta x)$. This is sufficient to show that the $\mathcal{O}(\Delta t^2)$ terms in (3.33) and (3.34) agree to $\mathcal{O}(\Delta t^2 \, \Delta x)$. This demonstrates the second order accuracy for the algorithm based on f-waves.

3.4 A modified Burgers' Equation

As an example of the algorithm presented in this chapter, we consider the nonlinear initial value problem

$$\begin{aligned}&\frac{\partial}{\partial t}q(t,x) + \frac{\partial}{\partial x}\left[(1+\sigma x)\frac{q^2}{2}\right] = 0\\ &q(t=0,x) = f(x), \quad x \in (-\infty,+\infty),\end{aligned} \tag{3.36}$$

where σ is taken to be a non-negative constant. Notice that if $\sigma = 0$ this PDE is simply Burgers' equation. In this example, we assume $f(x) > 0$ for all x and that $f'(x) < 0$ on some part of our computational domain. This guarantees that at some time $T_{\mathcal{S}} > 0$, characteristics of equation (3.36) will cross and the solution will shock. This will allow us to test the accuracy of the new algorithm for some time $T_{\mathcal{A}} < T_{\mathcal{S}}$ while the solution is still smooth. For $t > T_{\mathcal{S}}$ we can verify that the shock is captured with no numerical oscillations.

In order to test the accuracy of the new algorithm, we need an *exact* solution for all time $t < T_{\mathcal{S}}$. The method of characteristics can be applied to find the implicit solution

$$x = \frac{(\sigma\xi + 1)(2 + \sigma t f(\xi))^2}{4\sigma} - \frac{1}{\sigma} \tag{3.37}$$

$$q(t,x) = \frac{2f(\xi)}{2 + \sigma t f(\xi)}, \tag{3.38}$$

so that given any x and $t < T_{\mathcal{S}}$, a value for ξ is found by solving (3.37), which is then used in (3.38) to find $q(t,x)$. This classical solution to the initial value problem (3.36) exists for times in the interval $[0, T_{\mathcal{S}}]$, where

$$T_{\mathcal{S}} = \min_{\xi}\left[\frac{-2}{\sigma f(\xi) + 2f'(\xi)(1+\sigma\xi)}\right]. \tag{3.39}$$

In the example presented here we use the initial condition

$$f(x) = \alpha \exp\left[\left(\frac{x - x_0}{\omega}\right)^2\right], \tag{3.40}$$

so that the above assumptions are satisfied. A plot of this initial condition is shown in Figure 3.2(a) as a dashed line. Notice that is is non-negative, and has a region of negative slope as desired. The exact solution can then be computed for all $t < T_{\mathcal{S}}$ by solving the nonlinear, implicit equation (3.37) for ξ, and using this in equation (3.38). The exact solution, therefore, is only as accurate as the solution of (3.37), which we solve to machine precision.

In Figures 3.2(a) through 3.3(b) we present a calculation with $\sigma = 3/5$, $\alpha = 1$, $x_0 = 0$, and $\omega = 4/5$. In Figure 3.2(a), the exact solution has been compared to the computed solution at $t = 0.6 \approx 0.78\,T_{\mathcal{S}}$. At this time, we have done an error analysis of the new algorithm. Figure 3.3(a) contains the errors that the method makes in both the max norm and the one norm. A log-log plot of these errors can be found in Figure 3.3(b), where we

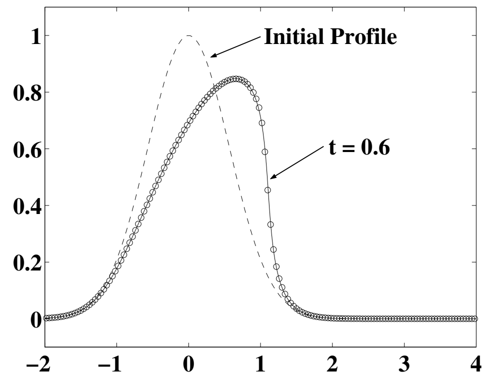

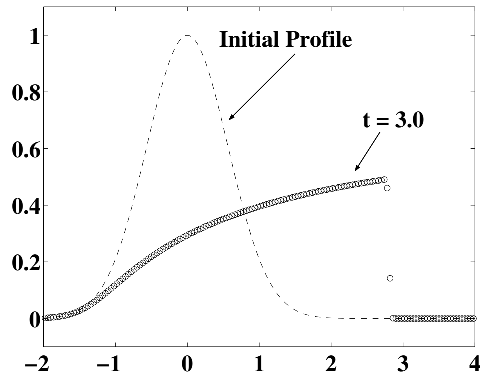

Figure 3.2: (a) A comparison between the exact solution (solid line) and a numerical solution (circles) at $t = 0.6 \approx 0.78T_b$. The solution is beginning to steepen as it propagates to the right. Also shown is the initial condition (dashed line). (b) The numerical solution at $t = 3.0$. The classical solution has shocked and we are computing the conservative weak solution. The dashed line, once again, represents the initial condition.

have plotted the one-norm errors with a circle and max-norm errors with an x. Also plotted is a linear fit to the errors from which an order of accuracy has been computed.

One thing to notice is that the one-norm errors are second order ($p = 1.98$), while the max-norm errors are slightly less than second order ($p = 1.76$). This is due to the fact that the solution is already quite steep at $t = 0.6$ (see Figure 3.2(a)), and errors in this steep region are dominant. The max norm is sensitive to these errors and will be slower to reach an asymptotic value for the order of accuracy.

In Figure 3.2(b) we show the numerical solution at $t = 3 > T_{\mathcal{S}}$. The classical solution no longer exists at this time. The circles represent the discontinuous weak solution to the conservation law (3.36). Notice the sharp resolution of the shock front, and the fact that there are no oscillations throughout the solution.

More examples of accuracy studies for the f-wave algorithm developed here can be found in [4], the paper on which this chapter is based. An accuracy study of the algorithm's performance for elastic waves in heterogeneous media is presented in Section 4 of [4], and for linear acoustics in Section 5.

3.5 Flow of an inviscid gas in a duct with varying cross-sectional area

In the following example, we investigate the performance of the algorithm for the flow of an inviscid gas in a duct with a cross-sectional area that is a function of the spatial variable. Other high-resolution schemes have been proposed for this system, for example in [16] a TVD scheme was proposed for this system including losses due to friction and heat transfer to the wall. In this section we neglect such losses and apply the algorithm to the flow of a

dx	$\|Q-q\|_\infty$	$\|Q-q\|_1$
0.04	2.226889e-02	3.696241e-03
0.02	7.376764e-03	9.555440e-04
0.01	2.199132e-03	2.386655e-04
0.005	5.712810e-04	6.031043e-05
order	1.76	1.98

(a)

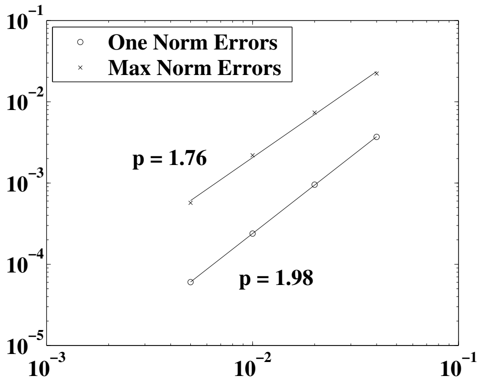

(b)

Figure 3.3: (a) Errors in the computed solution for various cell widths at $t = 0.6$.(b) A Log-Log plot of the error as a function of the cell width dx. The One norm is plotted with a circle and the Max norm is plotted with an x. A linear fit is also plotted from which an order of accuracy is computed.

perfect, one-dimensional fluid in a duct as depicted in Figure 3.4. The cross-sectional area, $a(x)$, represents the distance between symmetric walls that follow the function $f(x)$.

The quasi-one-dimensional equations that govern the unsteady flow in such a duct are the one-dimensional Euler equations with a source term that results from pressure forces on the duct walls. They can be written

$$\frac{\partial}{\partial t}\begin{pmatrix}\rho\\ \rho u\\ e\end{pmatrix}+\frac{1}{a(x)}\frac{\partial}{\partial x}\left[a(x)\begin{pmatrix}\rho u\\ \rho u^2+p\\ (e+p)\,u\end{pmatrix}\right]=\begin{pmatrix}0\\ \frac{a'(x)\,p}{a(x)}\\ 0\end{pmatrix}, \tag{3.41}$$

where the area $a(x)$ gives rise to a spatially-varying flux function. For steady flow in the duct, the conservation of mass (the first equation in (3.41)) suggests that the fluid must speed up as $a(x)$ gets smaller. It follows that there may exist a *critical* Mach number $\mathcal{M}^*$ at the inlet above which the flow will transition from a subsonic to supersonic flow as it passes through the constricted region of the duct. In order for the flow to return to a subsonic state, a stationary shock must be present with a location dependent on the pressure jump across the shock.

A good test for the algorithm presented in this chapter is to initialize an unsteady flow from left to right and apply boundary conditions that are consistent with a steady solution as mentioned above. After a period of unsteady flow, the numerical solution should settle into the correct steady solution. We present two such numerical calculations in this section. In the first calculation, we initialize a flow at the duct inlet with a velocity such that the Mach number $\mathcal{M}$ is below the critical value $\mathcal{M}^*$. The boundary conditions that are applied

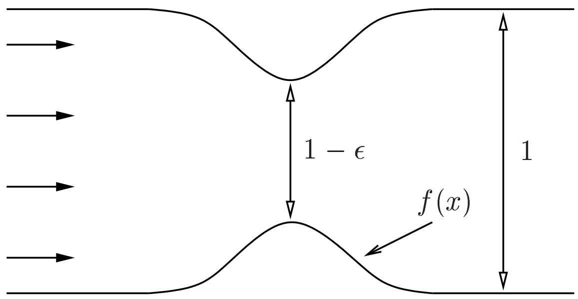

Figure 3.4: Flow in a duct with variable cross-sectional area. The wall is placed along the function $f(x)$. The minimum area is $a_{\min} = 1 - \epsilon$.

in this calculation are consistent with a subsonic flow so that the fluid remains subsonic everywhere, but with an increased velocity in the vicinity of the duct constriction shown in Figure 3.4. In the second calculation that we present the initial Mach number at the inlet is larger than the critical value, $\mathcal{M} > \mathcal{M}^*$. We also apply boundary conditions consistent with a stationary shock located at $x = 2.5$. In both cases we compare the numerical solution with an exact solution.

The exact solution can be derived using the fact that the fluid remains isentropic in smooth regions. If we define

$$\mathcal{G}(\mathcal{M}) = \mathcal{M} \left(\frac{\gamma + 1}{2 + (\gamma - 1)} \mathcal{M}^2 \right)^{\kappa}, \tag{3.42}$$

where γ is the polytropic index of the fluid and $\kappa = (\gamma + 1)/(2(\gamma - 1))$, then the isentropic nature of the flow in smooth regions is expressed by

$$a(x)\, \mathcal{G}(\mathcal{M}) = a(x_0)\, \mathcal{G}(\mathcal{M}_0), \tag{3.43}$$

where x_0 is the value of x at the left boundary and $\mathcal{M}_0 \equiv \mathcal{M}(x_0)$. To find $\mathcal{M}(x)$, we iterate to find $\mathcal{M}$ that satisfies the nonlinear equation

$$g(\mathcal{M}) \equiv \mathcal{F}(\mathcal{M}) - \frac{a(x_0)}{a(x)} \mathcal{F}(\mathcal{M}_0) = 0. \tag{3.44}$$

If $\mathcal{M}_0 > \mathcal{M}^*$ and there is a stationary shock in the duct as in Figure 3.5(b), then the Hugoniot jump conditions can be used to calculate the flow variables just to the right of the shock. After the shock the solution is once again smooth and will satisfy equation (3.44). Using the post-shock flow variables instead of the values at the left boundary, we can proceed with the iterative procedure to the right boundary (we assume only one shock since $f''(x)$ will not change sign in this example). Figures 3.5(a) and 3.5(b) show two such exact solutions (marked by an x) for the Mach number $\mathcal{M}(x)$ of a steady flow in a duct on

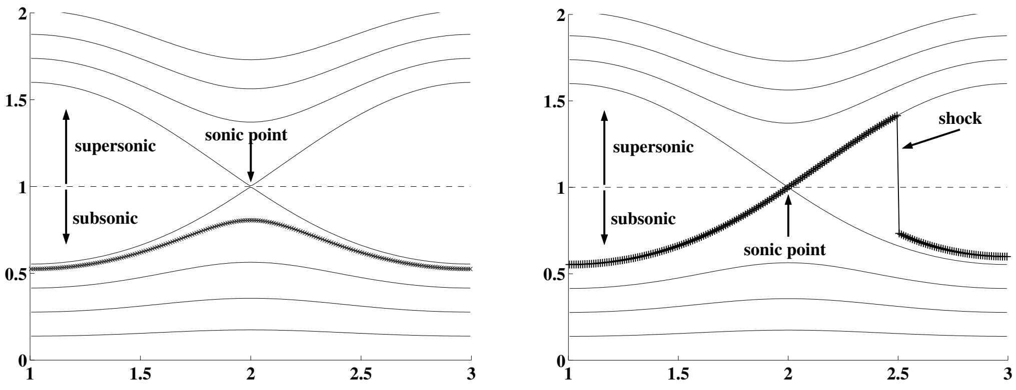

(a) subsonic (b) supersonic

Figure 3.5: The exact solution for flow in a duct with spatially-varying cross-sectional area. Plotted is the Mach number $\mathcal{M}(x)$ for (a) initial conditions so that the flow remains subsonic throughout the duct, and (b) initial conditions so that the flow becomes supersonic and a shock develops.

a domain $x \in [1, 3]$. The cross-sectional area of the duct has the form

$$a(x) = \begin{cases} 1 & \text{for } x < 1 \\ 1 + \frac{\epsilon}{2}\left[\cos \pi(x-1) - 1\right] & \text{for } 1 \le x \le 3 \\ 1 & \text{for } x > 3. \end{cases} \tag{3.45}$$

In both figures we have plotted several solutions with solid lines. Notice that as the Mach number at the inlet increases, the solution gets closer to the supersonic transition. In Figure 3.5(a) the marked solution remains subsonic throughout the domain. In Figure 3.5(b), however, there is a transition to supersonic flow and therefore stationary shock located at $x = 2.5$. These solutions can be used to compare with a numerical solution.

We now present the numerical solution generated by our algorithm and compare it with the exact solution for $a(x)$ defined by equation (3.45). The fluid is initialized to a uniform state in which the flow is from left to right. Boundary conditions are generated using the exact solutions discussed above and they are applied in each time step. Figures 3.6(a) and 3.6(b) show the time evolution of the numerical solution for the subsonic and supersonic problem, respectively. They depict the contours of the Mach number, $\mathcal{M}(x)$, in the x-t plane. Notice that both the subsonic solution (Figure 3.6(a)) and the supersonic solution (Figure 3.6(b)) are initially quite dynamic, but both eventually settle to a stationary solution. In the subsonic case, the Mach number remains smooth as expected. In the supersonic case, however, the shock develops around $t = 5$, moves around until about $t = 20$, and finally settles into the position at $x = 2.5$.

Figure 3.7 compares the density, velocity, and pressure of the exact (solid line) and

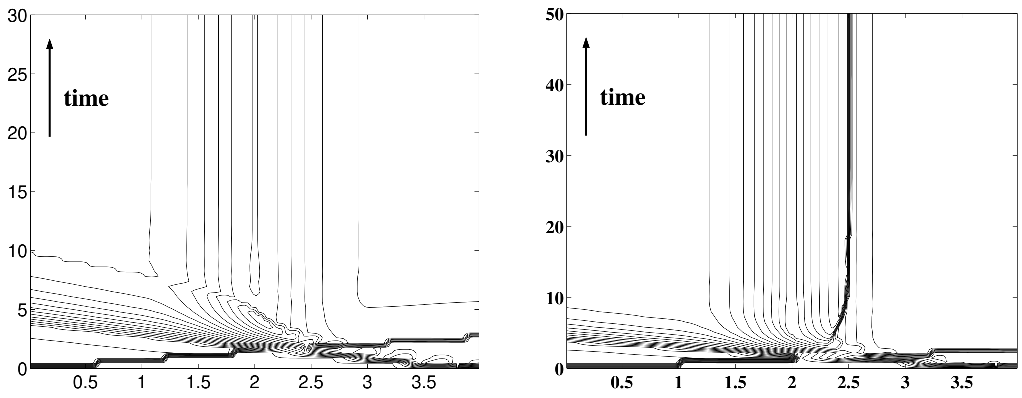

(a) subsonic

(b) supersonic

Figure 3.6: The time evolution of both the (a) subsonic solution and the (b) supersonic solution. Contours of the solution in the $x - t$ plane are shown. At early times both solutions are dynamic, but eventually settle to a steady-state.

numerical (circles) solution at the final time for the subsonic problem. In this calculation we have taken $\epsilon = 0.2$, and used 160 cells across the domain. As expected, the velocity of the fluid increases in the region where the area is small. The numerical solution captures the subsonic flow very well in all fields.

Finally, Figure 3.8 shows the same comparison for the supersonic problem. In this calculation the boundary conditions used were generated using the exact solution for a stationary shock located at $x = 2.5$ as shown in Figure 3.5(b). Once again, the numerical solution (circles) compares very well with the exact solution in all fields. It is important to note that the shock is not present in the initial data. It develops and then moves as time evolves as can be seen in Figure 3.6(b). Figure 3.8 demonstrates that the shock, in fact, moves to the correct location. The sharp resolution of both the shock strength and location can be seen in the density, velocity, and pressure.

3.6 Extension to higher dimensions

The algorithm based on f-waves presented in this chapter is easily extended to multidimensional conservation laws with spatially-varying flux functions of the form

$$\boldsymbol{q}_{,t} + \sum_{k=1}^{n_d} \boldsymbol{f}^{(k)}(\boldsymbol{q}, x^j)_{,k} = 0, \tag{3.46}$$

where, once again, braces around the k^{th} index indicate a vector along the x^k coordinate line and $j \in \{1, \cdots, n_d\}$. The procedure directly follows the extension of the standard wave propagation algorithm to multidimensional problems discussed in Section 2.3.2.

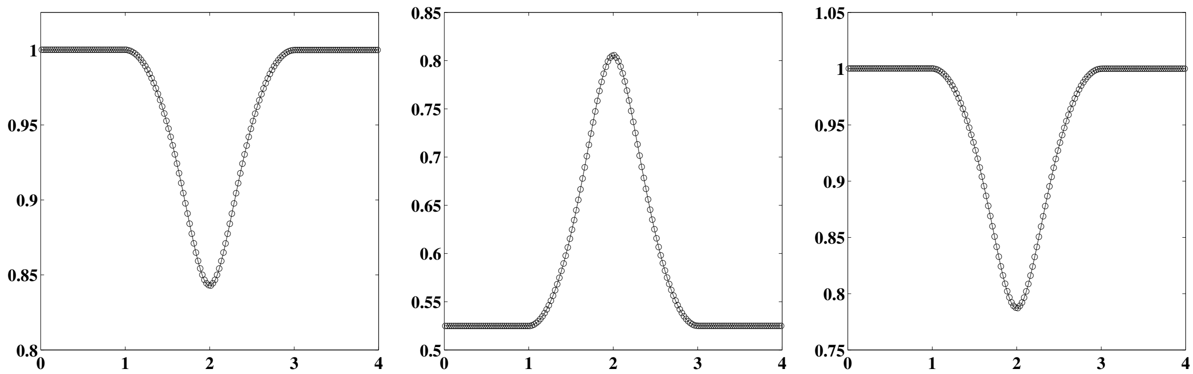

(a) density (b) velocity (c) pressure

Figure 3.7: A comparison of the numerical solution (circles) to the exact solution (solid line) for the entirely subsonic problem shown in Figure 3.5(a). Shown are the (a) density, (b) velocity, and (c) pressure for the flow.

If $n_d = 2$, for example, one-dimensional generalized Riemann problems are solved so that $\boldsymbol{f}_i(\boldsymbol{Q}_{i\,j}) - \boldsymbol{f}_{i-1}(\boldsymbol{Q}_{i-1\,j})$ is split into a sum of f-waves at each interface, all traveling along the x^i direction. These f-waves induce the left-going fluctuation $\boldsymbol{\mathcal{A}}_i^- \boldsymbol{\Delta Q}_{i-1/2\,j}$ and a right-going fluctuation $\boldsymbol{\mathcal{A}}_i^+ \boldsymbol{\Delta Q}_{i-1/2\,j}$ as before. These fluctuations are then split into eigenvectors of an approximation to the transverse Jacobian, in this case $\partial \boldsymbol{f}^{(j)} / \partial \boldsymbol{q}$.

An example of the algorithm discussed here applied to the multidimensional linear acoustic equations can be found in [4]. In fact, a multidimensional implementation of this algorithm based on f-waves is a key component in the development of a numerical algorithm for conservation laws on manifolds which is the main goal of this thesis. In Chapter 1 we claimed that a conservation law on a manifold has the form of equation (1.4), involving a spatially-varying flux function. In Chapter 5 we derive the form of the spatial variance induced by the manifold $\mathscr{M}$, and present examples of the implementation of this multidimensional algorithm in Chapters 6 and 8.

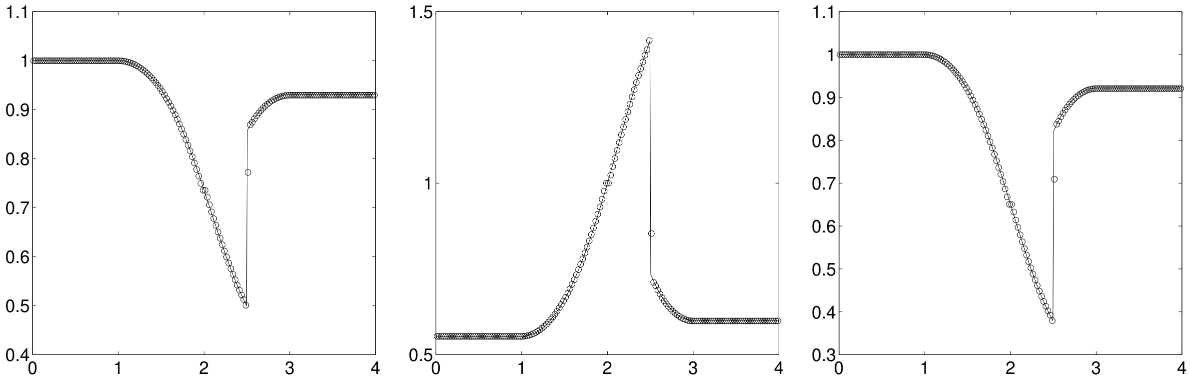

(a) density (b) velocity (c) pressure

Figure 3.8: A comparison of the numerical solution (circles) to the exact solution (solid line) for the supersonic problem shown in Figure 3.5(b). Shown are the (a) density, (b) velocity, and (c) pressure for the flow.